Comput Mech (2009) 44:669–682
DOI 10.1007/s00466-009-0396-1

ORIGINAL PAPER

Developments in the application of the generalized finite element method to thick shell problems

Oscar A. Garcia · Eduardo Alberto Fancello · Paulo de Tarso R. Mendonça

Received: 24 January 2008 / Accepted: 5 May 2009 / Published online: 4 June 2009

Abstract This paper develops and analyzes two techniques to extend the use of generalized finite element method techniques to structural shell problems. The first one is a procedure to define local domains for enrichment functions based on the use of *pseudo-tangent planes*. The second one is a procedure for imposing homogeneous essential boundary conditions and treatment of boundary layer problems by utilizing special functions. The main idea supporting the pseudo-tangent proposition is the separation of the geometric description, with its intrinsical distortions with respect to the physical domain, from the approximation space, which is defined in a locally undistorted domain. The treatment of essential boundary conditions allows an adequate enrichment in the boundary vicinity, preserving the completeness of the polynomials defining the basis functions. A set of numerical cases are tested in order to show the behavior of the proposed strategies, and a number of observations are drawn from the results, as follows. First, the technique of constructing the enrichment functions on a pseudo-tangent plane shows good results, even with strongly curved shell surfaces. With respect to the locking problem, the method behaves in a similar way as the classical hierarchical finite element methods, avoiding locking for appropriate levels of p-refinements. The procedure considered to impose essential boundary conditions in strong form appears to be more accurate than with the penalty or Lagrange multiplier methods. The inclusion of exponential modes for the treatment of boundary layers in shells provided extremely good results, even with integration elements much larger than the shell thickness.

O. A. Garcia · E. A. Fancello (✉) · P. de Tarso R. Mendonça
Departmento de Engenharia Mecânica,
Universidade Federal de Santa Catarina, Florianópolis, SC, Brazil
e-mail: fancello@grante.ufsc.br

Keywords Generalized finite elements · Meshless methods · Thick shells · Boundary layers

1 Introduction

Numerical modeling of complex problems in computational mechanics points towards meshless methods as a promising alternative in order to avoid excessive loss of accuracy due to mesh distortion and to provide more flexibility for the definition of the approximation spaces in comparison with the classical finite element method (FEM). Its advantages become more evident in problems involving singularities, boundary layer phenomena, impact, damage and failure in phase change situations.

Among the most known meshless methods one can mention: multiquadric [25,26]; reproducing kernel particle method (RKPM) [29]; element free Galerkin method (EFGM) [8]. The latter has the characteristic of naturally introducing a procedure to perform hp-adaptivity, avoiding the construction of functions by sophisticated hierarchical techniques in intrinsic coordinates. The advantages of these procedures are, however, balanced by the computational cost involved in the integration process, since each covering of each point is arbitrary. In order to ameliorate the cost of numerical integration and the implementation difficulties of mesh free methods, Oden et al. [35], proposed that, instead of using generalized spheres or rectangles for defining the local supports, it would be more convenient to use finite element meshes. Therefore, the support associated to a node would be built by the union of the elements connected to that node. In this way, the method becomes only partially meshfree: the mesh is utilized to define the partition of unity and to perform integration, but the enrichment functions are defined in global coordinates. This procedure led to the generalized

finite element method (GFEM) [16]. Independent developments were conducted by Babuska and Melenk [4], named as partition of unit finite element method (PUFEM) It also led to the works of Belytschko and Black [6] and Moes [32], named extended finite element method (XFEM).

For Peer Although excellent results are obtained by these methods for plane and tridimensional problems, few developments have been made for shell problems, and some technical aspects are still open to improvements. Among them, the imposition of essential boundary conditions, processing time and an adequate approach for arbitrary curved shell problems. The first contribution in this aspect was presented by Krysl and Belytschko [24], where the approximation space is constructed on a parameterized domain obtained from a moving least square (MLS) approximation of the real shell geometry (with geometry and displacement fields are approximated by the same functions). This technique shows a good behavior, although it demands appreciable efforts in order to generate the parameterized domain. Moreover, it does not support *p*- or *hp*-enrichments.

A different approach for non-linear thin shell problem was presented by Li et al. [28], where the authors use the 3-D RKPM. In this case a solid-type approach of the shell was used and the local shape functions have a spherical support.

Among the most recent works we should mention the paper of Liu et al. [27], who approximate the stress field in shear deformation model for shells utilizing a geometrically exact formulation. The basis functions in the radial direction utilized for the stresses are also utilized to approximate the reference surface. However, differently from the MLS functions utilized in EFGM, the radial basis of the conforming radial point interpolation method shows the Kronecker delta property.

Ferreira et al. [18], utilize a multiquadric basis function to obtain the natural frequencies of the shallow shell problem with laminated composite material and modeled by the first order theory of Donnel. The reference surface is not parameterized and the space of approximation is built in a single tangent plane.

In the present work, a GFEM procedure is proposed to deal with moderately thick shells. The shell geometry is treated following the degenerate solid strategy [1] while the approximation space is created by a combination of the Partition of Unity provided by the traditional element shape functions and local enrichment functions defined in global coordinates. This enrichment space is defined over specially constructed pseudo-tangent planes, whose normals are oriented along the thickness in the vertex of the associated solid elements.

The most used procedures to enforce essential boundary conditions consist in incorporating the boundary condition in weak form by means of Lagrange multipliers [8], penalty method [42], Nitsche's method [3,22] or by direct substitution of the boundary functions [28]. These techniques show good results, but present additional computational costs due to the integration on the Dirichlet portion of the boundary, or due to the matrix inversion needed to obtain the functions on the boundary. Besides, except for the direct substitution method, in general these methods are capable to impose the boundary conditions in an approximate way. Taking advantage of the GFEM characteristics, an alternative natural way to impose essential conditions is used here, based on special boundary functions for the PU and corresponding enrichments that strongly satisfy the needed conditions at the boundary. Another use of special functions is included in this work to the capture boundary layer phenomena in shell problems.

The paper is organized as follows: Sect. 2 is a general brief description of the GFEM method. Section 3 presents two different uses of special functions: essential boundary conditions and boundary layer representations. Section 4 develops approximation functions in curved surfaces and Sect. 5 applies the GFEM technique to a thick shell finite element model. Finally, Sect. 6 presents several numerical examples in which the following aspects are tested: the capacity of the proposed approach to deal with locking with uniform strategies of p-enrichment and the efficiency of this type of enrichment to capture boundary layer behavior in Reissner–Mindlin plates and shells.

2 Approximation space in GFEM

Formally, the GFEM approximation space is defined as follows. Let Ω be an open bounded domain and $\{\Omega_\alpha\}_{\alpha=1}^N$ a covering of compact sets defined by a domain partition. Consider also a Partition of Unity (PU) $\{\varphi_\alpha\}_{\alpha=1}^N$ of the Lipschitz type associated with this covering. At each set Ω_α of the covering (referred to in the text as *cloud*), a space Q_α is defined to represent the local enrichment functions over the cloud Ω_α. The global approximation space is then given, symbolically, by the expression:

$$Q = \sum_{\alpha=1}^{N} \varphi_\alpha Q_\alpha \tag{1}$$

where N is the number of clouds defining the support of the problem. Equation (1) means that the global approximation space is defined by functions obtained by the product of the PU functions with a set of appropriate enrichment functions. In this definition, the PU ensures the exact representation of constant functions while the enrichment takes into account higher order representations.

The global space Q built in this way inherits the approximation properties of the enrichment functions Q_α (See [30, Theorem 3.2]) which, in general, are built using polynomials due to their well known approximation properties. The set Q may also be redefined by the expression

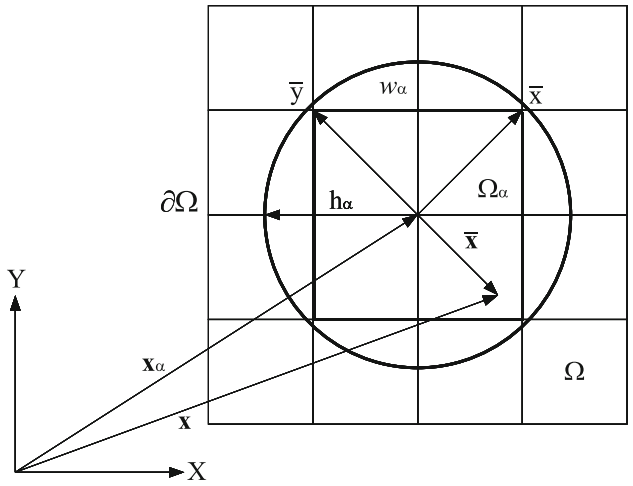

Fig. 1 Domain of the cloud Ω_α

$$Q = \text{span}\{\mathcal{F}_N^p\} \tag{2}$$

where $\mathcal{F}_N^p$ represents the set of global approximation functions. If the enrichment functions are obtained using the tensor product of polynomials, one has:

$$\mathcal{F}_N^p = \{\{\varphi_\alpha \bar{Q}_\alpha^p\} : 1 \leq \alpha \leq N\} \tag{3}$$

$$\bar{Q}_\alpha^p = \{L_{ij}(\bar{\mathbf{x}}) = \bar{x}^i \bar{y}^j : 0 \leq i, j \leq p, i, j \geq 0, p \geq 0\} \tag{4}$$

If complete polynomials are used instead (triangle of Pascal),

$$\mathcal{F}_N^p = \left\{\left\{\varphi_\alpha \hat{Q}_\alpha^p\right\} : 1 \leq \alpha \leq N\right\} \tag{5}$$

$$\hat{Q}_\alpha^p = \left\{L_{ij}\left(\bar{\mathbf{x}}\right) = \bar{x}^i \bar{y}^j : 0 \leq i, j \leq p, 0 \leq i + j \leq p\right\} \tag{6}$$

The spaces thus obtained are such that $P \subset Q$, where P is the set of polynomials of degree $g \leq p$.

Consider the relative position vector $\bar{\mathbf{x}} = [R]_\alpha^T(\mathbf{x} - \mathbf{x}_\alpha)$, where $\mathbf{x}$ represent the location of a point in global coordinates, $[R]_\alpha$ and $\mathbf{x}_\alpha$ are the rotation matrix and the position vector of the center of cloud Ω_α, respectively. Consider the normalized coordinate ξ associated with a circle of radius h_α (Fig. 1), such that:

$$\xi = \frac{\bar{\mathbf{x}}}{h_\alpha} \Longrightarrow \bar{\mathbf{x}} = h_\alpha \xi \tag{7}$$

Let $[-1, 1] \times [-1, 1] \in R^2$ be a normalized domain. The local enrichment functions are defined by:

$$L_{ij}\left(\bar{\mathbf{x}}\right) = \hat{L}_{ij}\left(\xi\right) \Longrightarrow \nabla_{\bar{\mathbf{x}}} L_{ij}\left(\bar{\mathbf{x}}\right) = \frac{1}{h_\alpha} \nabla_\xi \hat{L}_{ij}\left(\xi\right) \tag{8}$$

where $\hat{L}_{ij}(\xi)$ e $\nabla_\xi \hat{L}_{ij}(\xi)$ are the enrichment functions and their derivatives defined over the normalized domain.

This enrichment may also be performed along preferential directions in a straightforward way. A possible strategy is presented in [17]. In this case, an orthotropic set $\tilde{Q}_\alpha^p$, is obtained from the enrichment polynomial basis $\hat{Q}_\alpha^p$ and $\bar{Q}_\alpha^p$, defined in (6) and (4), such that the set of functions $\tilde{Q}_\alpha^p$ corresponding to a cloud α is defined by:

$$Q_\alpha^{(p_{\bar{x}}, p_{\bar{y}})} = \hat{Q}_\alpha^{p\,\max} \cap \bar{Q}_\alpha^{(p_{\bar{x}}, p_{\bar{y}})}$$

where $p\max = \max\left\{p_{\bar{x}}, p_{\bar{y}}\right\}$.

The following important characteristics of this method should be pointed out:

a) It provides limited cardinality because the number of supports covering each integration point is known beforehand;
b) It is possible to enforce essential boundary condition in strong form;
c) It is possible to define directional anisotropic p -enrichments easily;
d) It allows the combination of classical polynomial bases with special built functions that belong to particular solutions of the problem;
e) Semi-definite stiffness matrices may arise when the partition of unity and the enrichment functions are both polynomials.

A well known technical drawback that appears when both the partition of unity and the enrichment functions are polynomials is that the stiffness of the matrix becomes semi-definite which causes difficulties in solving the linear system. Fortunately, this inconvenience is tractable and in the present study the procedure proposed in [16] is used.

3 Special functions

One of the main attractive features of meshless and GFEM methods is their flexibility, allowing the incorporation of customized functions for specific tasks. In this research two different special functions are proposed. The first group deals with essential boundary conditions, while the second group provides appropriate enrichment functions in order to capture boundary layer phenomena.

3.1 Special functions for essential boundary conditions

The development of efficient and low cost methods to enforce essential boundary conditions still constitutes a challenge in relation to meshless methods. In general, they use radial supports whose approximation functions do not possess the selective property of Kronecker Delta. In these cases, essential boundary conditions are enforced by penalization or Lagrange multiplier techniques. These procedures may generate small oscillations in the fields at the prescribed boundary and therefore are, in general, not adequate to represent problems of localization over these contours. Some alterna-

tives have been presented like the use of singular weighting functions [15] and the modification of the functions on the Dirichlet boundary [28]. In the first case, the results are exact for the clouds associated with the singular weighting functions. However, the results oscillate at points at a distance of the cloud, and the integration of these functions by quadrature is still a delicate process. The second alternative gives exact values at the prescribed boundary but with high computational cost, comparable with that of the integration on the boundary used in the Lagrange and penalty methods.

In the case of GFEM, the partition of unity functions possess the Kronecker delta property which, at a first sight, enables boundary conditions to be imposed in the same way as in classical FEM. However, the basic concept of enforcing a homogeneous Dirichlet boundary condition through the elimination of the PoU functions (and their enrichments) associated with the prescribed boundaries may provide incorrect results, since the space generated is precisely conforming but not minimally conforming (see Szabó and Babuska [36]). This phenomenon was registered by Schwebke and Holzer [37] for the problem of plane elasticity with p-enrichment. In the present case, the set of approximation functions has finite deformation energy, but it is not complete. This limitation is critical in bending problems approximated by p-refinement with a small number of elements, as is shown in the following example.

Consider the bending of a rectangular plate with soft simple supports on two opposite sides, as in Fig. 2. The plate has the following characteristics: length $L = 10$ mm, width $b = 2$ mm, thickness $t = 1$ mm, elasticity modulus $E = 2.1 \times 10^5$ MPa and uniformly distributed load $q = 0.1$ MPa. The domain is modelled with two square Q8 Reissner–Mindlin type elements, as indicated in Fig. 2. The Poisson coefficient is zero in order to use the Euler-Bernoulli analytical solution of beams as the reference value.

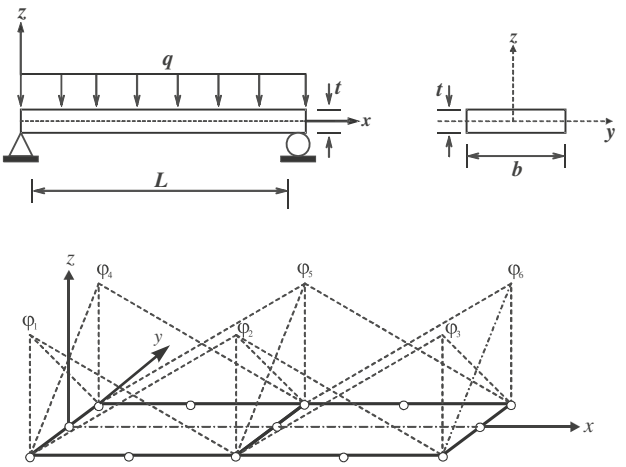

Fig. 2 Plate simply supported at opposite edges, modeled by 2×1 Q8 elements

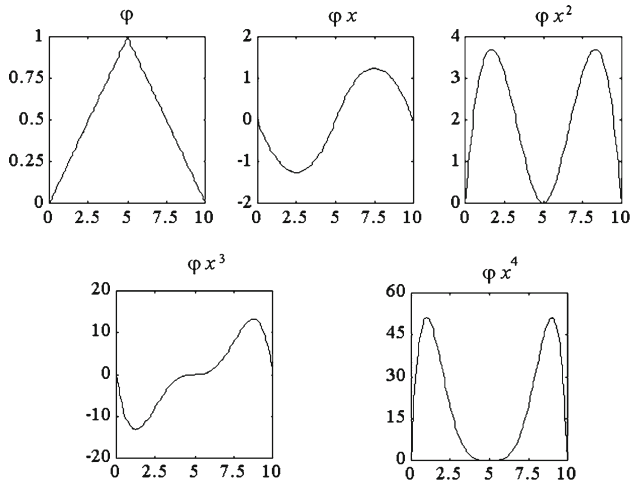

Fig. 3 Trace of the functions associated with cloud $\alpha = 2$, over the boundary $(x, -1)$

The approximation space for transverse displacement w was built according to Eqs. (5) and (6), for $N = 6$ and $p = 4$. In order to satisfy the essential boundary conditions, the local functions associated with the clouds over the restricted parts of the boundary were eliminated. Therefore, the resulting space is defined by:

$$\mathcal{F}_{N=6}^{p=4} = \left\{ \begin{array}{l} \left\{ \varphi_\alpha \hat{Q}_\alpha^p \right\}, \quad 1 \leq \alpha \leq N, \\ \varphi_1 \hat{Q}_1^p \equiv \varphi_3 \hat{Q}_3^p \equiv \varphi_4 \hat{Q}_4^p \equiv \varphi_6 \hat{Q}_6^p \equiv 0 \end{array} \right\} \tag{9}$$

The traces of the approximation functions corresponding to the cloud $\alpha = 2$, for the points at coordinates $(x, -1)$ are shown in Fig. 3. The solution is symmetric with relation to $x = 5$, such that only the even functions φ_2, $\varphi_2 x^2$ and $\varphi_2 x^4$ are useful in representing the transverse displacement w. Therefore, the set lacks quadratic and quartic terms. Utilizing these functions, the solution obtained (shown in Fig. 4a) is qualitatively different from the correct solution obtained by the penalty method (Fig. 4b).

The procedure here proposed imposes boundary conditions in strong form by substituting PU functions on the boundary with special functions which vanish at this boundary (Garcia [21]). These new functions, denominated *boundary functions*, are obtained by a multiplicative restriction procedure, similar to that proposed by Schwebke and Holzer [37]. These functions are obtained through the tensor product of the PU functions associated with the prescribed degree of freedom, and *ramp functions* defined in the element domain. The ramp function has the same support as the clouds on the prescribed boundary, and is defined for each degree of freedom in the boundary. Consequently, the number of ramp functions per element on the prescribed boundary is always equal to the number of prescribed degrees of freedom in the model. The construction of these functions is extremely simple and shown by the following example.

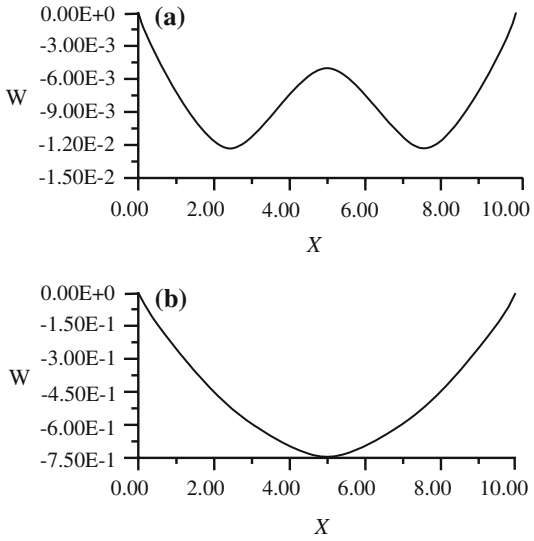

Fig. 4 **a** Modes obtained considering incomplete space; **b** modes obtained by the penalty method

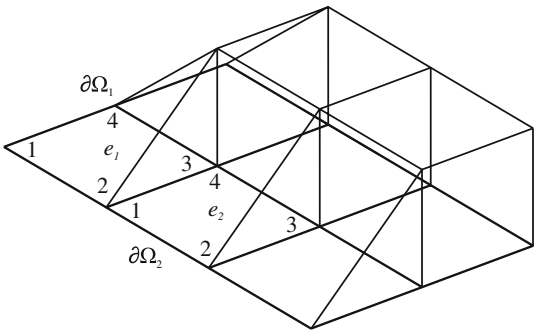

Fig. 5 Prescribed boundary segment and ramp function corresponding to the prescribed degrees of freedom

Consider the domain Ω depicted in Fig. 5, with essential homogeneous conditions on the boundaries $\partial\Omega_1$ and $\partial\Omega_2$ for an arbitrary degree of freedom u. The ramp function $\mathcal{R}_u(\xi, \eta)$ associated with u is defined as the summation of the PoU functions at the clouds whose nodes are not situated on the prescribed boundaries. Taking, for example, the elements e_1 and e_2 with sides on the prescribed boundaries, the ramp function is constructed as indicated in Table 1.

With the ramp function already calculated, a set of boundary functions is defined for those clouds whose central nodes are located at the prescribed borders. The functions are obtained from the product of the ramp function and the partition

Table 1 Ramp functions associated with elements with boundaries on $\partial\Omega_1 \cup \partial\Omega_2$

Element	1	2	3	4	$\mathcal{R}_u(\xi, \eta)$
1	1	1	0	1	$\varphi_3(\xi, \eta)$
2	1	1	0	0	$\varphi_3(\xi, \eta) + \varphi_4(\xi, \eta)$

Table 2 Tensor product of ramp functions and the partition of unity corresponding to the prescribed degrees of freedom

Element	Node	$\mathcal{R}_u(\xi, \eta)$	$\mathcal{B}_u(\xi, \eta)$
1	1	φ_3	$\varphi_1\varphi_3$
1	2	φ_3	$\varphi_2\varphi_3$
2	1	$\varphi_3 + \varphi_4$	$\varphi_1(\varphi_3 + \varphi_4)$
2	2	$\varphi_3 + \varphi_4$	$\varphi_2(\varphi_3 + \varphi_4)$

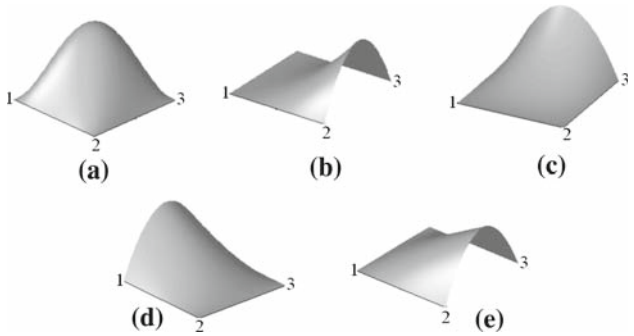

Fig. 6 Boundary functions of element 1: **a** node 1; **b** node 2; **c** node 4. Boundary functions of element 2: **d** node 1; **e** node 2

of unity associated to the nodes at the Dirichlet border. The boundary function is obtained easily at the element level as exemplified in Table 2 for the elements e_1 and e_2 of Fig. 5.

Figure 6a–c show the boundary functions associated with element e_1 and Fig. 6d and e show the boundary functions of element e_2.

Finally, once the boundary functions are constructed for the clouds with prescribed degrees of freedom, the PU associated with the cloud is substituted by this function, together with all its products with the enrichments.

It is verified that, applying the proposed technique to the example of Fig. 2, the correct solution is recovered.

3.2 Special functions for boundary layers

In plates and shallow shells modeled by the Reissner–Mindlin model, a boundary layer phenomenon is usually developed in the form of an exponential response along a region between the boundary and a distance of about the size of the thickness. Denoting ω and ϕ the transverse displacement and rotation fields of the Reissner–Mindlin model, respectively, and writing them by means of asymptotic expansions with respect to the thickness t, one obtains the expressions [2]:

$$\omega \sim \omega_0 + t\omega_1 + t^2\omega_2 + \cdots \tag{10}$$

$$\phi \sim \left(\phi_0 + t\phi_1 + t^2\phi_2 + \cdots\right) + \chi\left(\Phi_0 + t\Phi_1 + t^2\Phi_2 + \cdots\right) \tag{11}$$

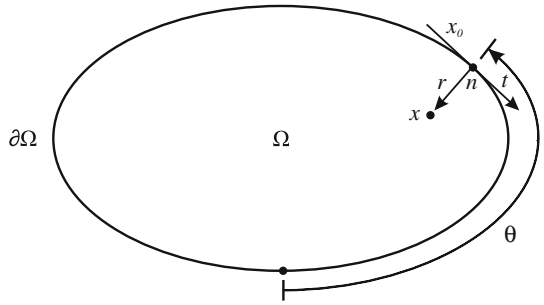

Fig. 7 Curvilinear coordinates for special functions

In expressions (10) and (11) the functions w_i and ϕ_i, with $i = 0, 1, 2, \ldots$, are smooth. The symbol χ represent an indicator operator whose value is zero for material points far enough from the boundary, and is equal to one for material points close enough to it. The functions Φ_i, with $i = 0, 1, 2, \ldots$, are exponential functions depending on the variables (r, θ), for a given thickness t, with the form

$$\Phi_i(r, \theta) = e^{-\beta r/t} F_i(r/t, \theta) \tag{12}$$

where k is the shear factor coefficient, r is the normal distance of a point to the boundary and θ is the curvilinear coordinate, as indicated in Fig. 7. The coefficient $\beta = \sqrt{12k}$ is characteristic of the Mindlin plate model. Functions $F_i(r)$ are smooth for a given thickness t. When $t \to 0$ it follows that $w \to w_0$ and $\phi \to \phi_0 + \chi \Phi_0$.

These particular functions can be used to enrich the spaces at the boundaries. The proposition consists of approximating w and the smooth parts of ϕ in Ω with polynomial functions and approximating $\Phi(r, \theta)$ in $\partial\Omega$ with functions of the type (12). The set Q_α^p of smooth functions may be obtained from (4) or (6) while the set $\mathcal{V}_\alpha$ that provides the local exponential behavior is defined by

$$\mathcal{V}_\alpha = \{e^{-\beta r/t} F_\alpha(r/t, \theta), \quad F_\alpha \in P\} \tag{13}$$

In the present study the set $P = \{1, r, r^2, \ldots, r_n^{n-1}\}$, along with r and θ, are shown in Fig. 7. In this way, the global approximation function Q is redefined as:

$$Q = \sum_{\alpha=1}^{N} \varphi_\alpha \mathcal{V}_\alpha, \quad \text{with} \quad \mathcal{V}_\alpha \subset H^1_{(\Omega_\alpha \cap \Omega)} \tag{14}$$

$$\mathcal{V}_\alpha = \text{span}\left\{Q_\alpha^p \cup \chi V_\alpha\right\}, \tag{15}$$

where χ indicates whether the center of the cloud $\mathbf{x}_\alpha$ belongs to the enriched boundary

$$\chi = \begin{cases} 1 & \text{if } \mathbf{x}_\alpha \in \partial\Omega, \\ 0 & \text{if } \mathbf{x}_\alpha \notin \partial\Omega, \end{cases} \tag{16}$$

Figure 8 shows a local orthotropic enrichment obtained from the product of a smooth function $F(\xi, \eta)$ and an exponentially decaying function:

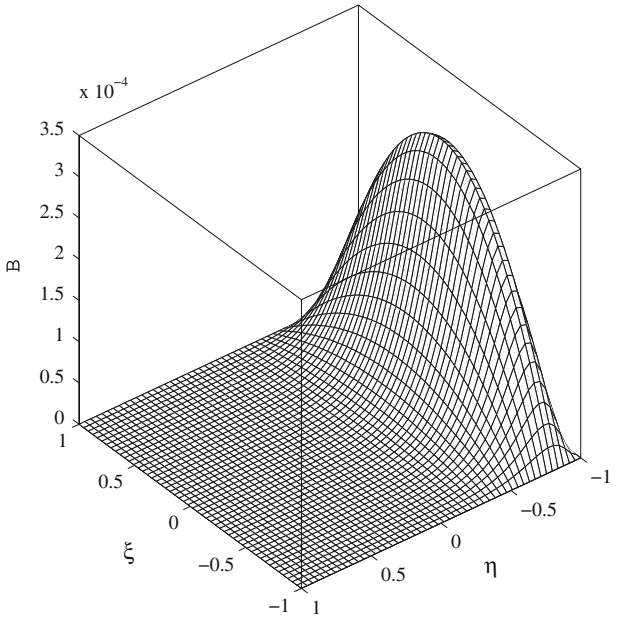

Fig. 8 Function with exponential decay in direction η associated with a cloud centered in $(0, -1)$

$$F(\xi, \eta) = \frac{1}{16}(1 + \xi)^2(1 - \eta)^2 \tag{17}$$

$$B(\xi, \eta) = F(\xi, \eta) e^{-\beta r/t}, \quad r(\xi, \eta) = \eta \tag{18}$$

Function $B(\xi, \eta)$ is defined on the domain

$$\Omega_e = \left\{\xi, \eta \in R^2 \mid -1 \le \xi \le 1, \ -1 \le \eta \le 1\right\} \tag{19}$$

and the cloud is centered at $(0, -1)$. Figure 8 shows a typical case where the behavior to be represented has a high gradient in the normal direction compared to that of the tangent direction.

4 Approximation functions in curved surfaces

In the classical FEM approach, each element is attached to a curvilinear coordinate system associated with its particular mapping. In the GFEM approach, a unique continuous mapping for each cloud (in this case a patch of elements) is necessary in order to define the approximation space on the curved shell. A possible strategy consists of using an approximation of the reference surface defined as in [24,27]. In the present paper, however, this concept is substituted by a local approximation based on pseudo-tangent planes. In order to detail this concept, consider a cloud formed by a patch of elements attached to a vertex point $\mathbf{X}_\alpha$. At this point define an orthonormal basis $[\theta_\alpha^1 \vdots \theta_\alpha^2 \vdots \mathbf{v}_{\alpha 3}]$ such that the vector $\mathbf{v}_{\alpha 3}$ is aligned with the vector normal (or pseudo-normal) to the shell surface (see Fig. 9). The remaining vectors $\theta_\alpha^1, \theta_\alpha^2$ define a pseudo-tangent plane π_α that is used to mediate the con-

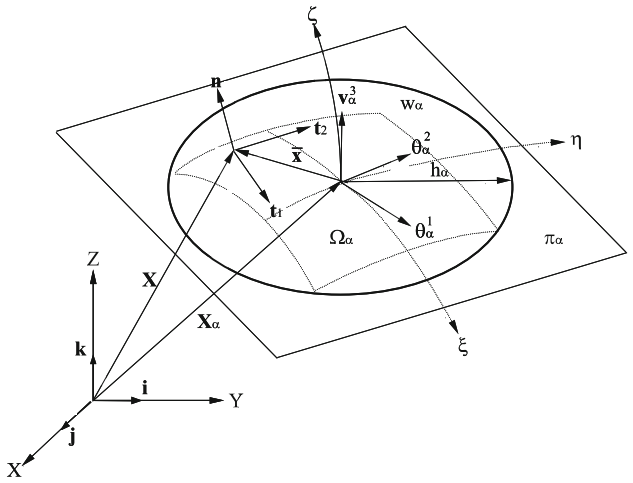

Fig. 9 Pseudo-tangent plane corresponding to the cloud $\mathbf{X}_\alpha$

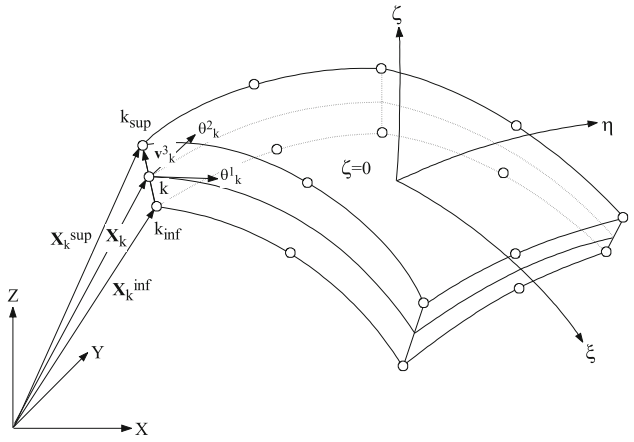

Fig. 10 Geometric characteristics of the degenerate solid [1]

struction of continuous enrichment functions over the cloud. In this plane, a circle of radius h_α and center $\mathbf{X}_\alpha$ contains the projection of all the points belonging to the cloud. The local support of the enrichment functions is then defined as

$$\omega_\alpha = \{\bar{\mathbf{x}}(\bar{x}, \bar{y}) \in R^2 : \|\bar{\mathbf{x}}\|_{R^2} \leq h_\alpha\} \tag{20}$$

$$\bar{\mathbf{x}} = \mathbf{P}_\alpha \mathbf{R}_\alpha^T (\mathbf{X} - \mathbf{X}_\alpha) \tag{21}$$

The projection operator $\mathbf{P}_\alpha$ is a defined by:

$$\mathbf{P}_\alpha = \begin{bmatrix} 1/h_\alpha & 0 & 0 \\ 0 & 1/h_\alpha & 0 \\ 0 & 0 & 0 \end{bmatrix} \tag{22}$$

and $\mathbf{R}_\alpha = [\theta_\alpha^1 \vdots \theta_\alpha^1 \vdots \mathbf{v}_{\alpha 3}]$ is the rotation matrix associated with the local basis of the cloud α in relation to the global coordinates.

The enrichment functions L_α defined in (4), (6) or (15) are dependent on the local coordinates $\bar{\mathbf{x}}$ on the pseudo-tangent plane ass seen in (20). Therefore, for a point belonging to an element attached to the vertex $\mathbf{X}_\alpha$ at elementar intrinsic coordinates (ξ, η), the enrichment functions and their gradients at this point are defined by:

$$L_\alpha(\xi, \eta) = L_\alpha(\bar{\mathbf{x}}(\xi, \eta)) \tag{23}$$

$$\nabla_\xi L_\alpha(\xi, \eta) = \mathbf{P}_\alpha \mathbf{R}_\alpha \mathbf{J}\, \nabla_{\bar{x}} L_\alpha(\bar{\mathbf{x}}(\xi, \eta)) \tag{24}$$

where $\nabla_{\bar{x}}$ is the gradient operator related to the local coordinates $\bar{\mathbf{x}}$ defined on the cloud α and $\mathbf{J}$ is the Jacobian matrix of the element mapping containing the point. Once both sets of functions for the enrichment are obtained in the elementar domain, the local approximation space is generated, computing the functions $\psi_k^\alpha(\xi, \eta) \in \mathcal{F}_N^p$ defined in (3) or (5).

5 A Mindlin–Reissner GFEM model

Different shell models may be used in conjunction with the method proposed above. In the following, a model based on a degenerate solid element and the Mindlin–Reissner cinematic approach is tested.

The degenerate solid element was introduced by Ahmad et al. [1] and since then it has been widely used in shell simulations using the FEM, different from to the formulations based on shell theories. The concept of degeneration is developed enforcing indeformability in the normal direction and allowing transverse shear deformation in the shell element. In this study the serendipity solid element with 16 nodes degenerates to an 8-node surface element, here denoted $Q8$, as depicted in Fig. 10.

At each node on the surface element, the pseudo-normal vector $\mathbf{v}_{3k}$ is defined by the coordinates of the upper (k_{sup}) and lower (k_{inf}) points across the thickness (see Fig. 10):

$$\mathbf{V}_{3k} = \mathbf{x}_k^{\text{sup}} - \mathbf{x}_k^{\text{inf}}, \quad \mathbf{v}_{3k} = \frac{\mathbf{V}_{3k}}{\|\mathbf{V}_{3k}\|} \quad \text{and} \quad \mathbf{V}_{3k} = \mathbf{v}_{3k} t_k \tag{25}$$

where t_k is the thickness measured along the edge. The other vectors of the basis, θ_k^1 and θ_k^2 (Fig. 10), are obtained from the tensor product of $\mathbf{v}_{3k}$ and the unit vectors $\mathbf{i}$, $\mathbf{j}$, $\mathbf{k}$ of the cartesian global coordinate system. Formally (considering that $\mathbf{j}$ is not parallel to $\mathbf{v}_{3k}$) one has:

$$\theta_k^1 = \frac{\mathbf{j} \times \mathbf{v}_{3k}}{\|\mathbf{j} \times \mathbf{v}_{3k}\|} \quad \text{and} \quad \theta_k^2 = \frac{\mathbf{v}_{3k} \times \theta_k^1}{\|\mathbf{v}_{3k} \times \theta_k^1\|}$$

The geometric mapping function of the element is then defined as:

$$\mathbf{x}(\xi, \eta, \zeta) = \sum_{k=1}^{n} \mathcal{N}_k(\xi, \eta)\mathbf{x}_k + \sum_{k=1}^{n} \mathcal{N}_k(\xi, \eta)\frac{t_k}{2}\mathbf{v}_{3k}\zeta \tag{26}$$

where n corresponds to the number of nodes on the reference surface of the element, $\mathcal{N}_k(\xi, \eta)$ are the lagrangian or

serendipty functions associated with nodes k on the reference surface, and (ξ, η, ζ) are the natural coordinates, such that $-1 \leq (\xi, \eta, \zeta) \leq 1$.

Let *active nodes* denote the nodes associated with the approximation functions. In the present case these nodes are at the vertices of the elements. Let n_n be the number of active nodes and n_α the number of approximation functions associated with each node. The total number of approximation functions is then (considering for simplicity the same number n_α for all nodes) $n_s = n_n n_\alpha$. Thus, the Reissner–Mindlin kinematic model provides the following decomposition of the displacement vector $\mathbf{u}$:

$$\mathbf{u}(\xi,\eta,\zeta) = \sum_{k=1}^{n_s} \left[\psi_k(\xi,\eta) \begin{Bmatrix} u_k \\ v_k \\ w_k \end{Bmatrix} + \psi_k(\xi,\eta) \frac{t_k}{2} \zeta \begin{bmatrix} \theta^1_{kx} & -\theta^2_{kx} \\ \theta^1_{ky} & -\theta^2_{ky} \\ \theta^1_{kz} & -\theta^2_{kz} \end{bmatrix} \begin{Bmatrix} \alpha_k \\ \beta_k \end{Bmatrix} \right] \tag{27}$$

where (u_k, v_k, w_k) are the displacement contributions of node k at the reference surface (in global coordinates), $\psi_k(\xi, \eta)$ and α_k, β_k are rotation angles of the pseudo-normal about the vectors θ^1_k and θ^2_k, respectively. Considering the kinematic model represented by (27), the displacement field can be written in matrix form as $\mathbf{u}_{h(k)} = \mathbf{N}_k \mathbf{U}_k$, where

$$\mathbf{N} = \begin{bmatrix} .. & \psi_k & 0 & 0 & \psi_k(\xi,\eta)\frac{t_k}{2}\zeta\theta^1_{kx} & -\psi_k(\xi,\eta)\frac{t_k}{2}\zeta\theta^2_{kx} & .. \\ .. & 0 & \psi_k & 0 & \psi_k(\xi,\eta)\frac{t_k}{2}\zeta\theta^1_{ky} & -\psi_k(\xi,\eta)\frac{t_k}{2}\zeta\theta^2_{ky} & .. \\ .. & 0 & 0 & \psi_k & \psi_k(\xi,\eta)\frac{t_k}{2}\zeta\theta^1_{kz} & -\psi_k(\xi,\eta)\frac{t_k}{2}\zeta\theta^2_{kz} & .. \end{bmatrix}$$

is the kinematic matrix and

$$\mathbf{U}^T = \{ \cdots \quad u_k \quad v_k \quad w_k \quad \alpha_k \quad \beta_k \quad \cdots \} \tag{28}$$

is the vector containing the displacement parameters and T denotes the matrix transpose. The gradient of displacements may be reorganized in the array $\mathbf{D}_\xi$:

$$\mathbf{D}^T_\xi = \left\{ \frac{\partial u}{\partial \xi} \quad \frac{\partial u}{\partial \eta} \quad \frac{\partial u}{\partial \zeta} \quad \frac{\partial v}{\partial \xi} \quad \frac{\partial v}{\partial \eta} \quad \frac{\partial v}{\partial \zeta} \quad \frac{\partial w}{\partial \xi} \quad \frac{\partial w}{\partial \eta} \quad \frac{\partial w}{\partial \zeta} \right\} \tag{29}$$

which can be calculated by the matrix operation $\mathbf{D}_\xi(\mathbf{u}) = \mathbf{G}\mathbf{U} = \partial_\xi \mathbf{N}\mathbf{U}$, where $\mathbf{G} = \partial_\xi \mathbf{N}$ is the gradient matrix and ∂_ξ a differential operator:

$$\partial^T_\xi = \begin{bmatrix} (\cdot)_{,\xi} & (\cdot)_{,\eta} & (\cdot)_{,\zeta} & 0 & 0 & 0 & 0 & 0 & 0 \\ 0 & 0 & 0 & (\cdot)_{,\xi} & (\cdot)_{,\eta} & (\cdot)_{,\zeta} & 0 & 0 & 0 \\ 0 & 0 & 0 & 0 & 0 & 0 & (\cdot)_{,\xi} & (\cdot)_{,\eta} & (\cdot)_{,\zeta} \end{bmatrix} \tag{30}$$

Therefore, the gradient with respect to global coordinates is obtained by $\mathbf{D}_\mathbf{X} = \bar{\mathbf{J}}\, \mathbf{D}_\xi(\mathbf{u}) = \bar{\mathbf{J}} G U$, where the Jacobian operator $\mathbf{J}$ is defined by:

$$\bar{\mathbf{J}} = \begin{bmatrix} \mathbf{J}^{-1} & 0 & 0 \\ 0 & \mathbf{J}^{-1} & 0 \\ 0 & 0 & \mathbf{J}^{-1} \end{bmatrix} \quad \text{and} \quad \mathbf{J} = \begin{bmatrix} X_{,\xi} & Y_{,\xi} & Z_{,\xi} \\ X_{,\eta} & Y_{,\eta} & Z_{,\eta} \\ X_{,\zeta} & Y_{,\zeta} & Z_{,\zeta} \end{bmatrix} \tag{31}$$

Since the numerical integration is performed within the element domain, it is convenient to define an orthogonal coordinate system $\hat{\mathbf{X}}$ associated with each integration point. Therefore the gradient with respect to this local system is calculated as follows:

$$\mathbf{D}_{\hat{\mathbf{X}}}(\mathbf{u}) = \mathcal{R}\mathbf{D}_\mathbf{X}(\mathbf{u}) \quad \text{i.e.,} \quad \mathbf{D}_{\hat{\mathbf{X}}}(\mathbf{u}) = \mathcal{R}\bar{\mathbf{J}}\mathbf{G}\mathbf{U} \tag{32}$$

The rotation operator $\mathcal{R}$, with 9×9 components, is calculated at the integration point using the rotation matrix $\mathbf{R} = [\mathbf{t}_1 \vdots \mathbf{t}_2 \vdots \mathbf{n}]$, (Fig. 9):

$$\mathcal{R}_i = \begin{bmatrix} t_{1x}\mathbf{R}^T & t_{1y}\mathbf{R}^T & t_{1z}\mathbf{R}^T \\ t_{2x}\mathbf{R}^T & t_{2y}\mathbf{R}^T & t_{2z}\mathbf{R}^T \\ n_x\mathbf{R}^T & n_y\mathbf{R}^T & n_z\mathbf{R}^T \end{bmatrix} \tag{33}$$

With the displacement derivatives calculated, the deformation components in coordinates $\hat{\mathbf{X}}$ are given by $\hat{\varepsilon} = \mathbf{H}\mathcal{R}\bar{\mathbf{J}}\mathbf{G}\mathbf{U} = \hat{\mathbf{B}}\mathbf{U}$, where $\hat{\mathbf{B}} = \mathbf{H}\mathcal{R}\bar{\mathbf{J}}\mathbf{G}$ and $\mathbf{H}$ is an adequate boolean matrix. Finally, the stiffness matrix used in the numerical quadrature is computed in the standard way as:

$$\mathbf{K}_e = \sum_{i=1}^{N_i} \hat{\mathbf{B}}^T_i \mathbf{C} \hat{\mathbf{B}}_i \det J_i \; W_\xi W_\eta W_\zeta \tag{34}$$

where N_i is the number of quadrature points in the element, $\mathbf{C}$ is the material constitutive matrix; W_ξ, W_η and W_ζ are the weights at the curvilinear coordinates ξ, η and ζ.

6 Numerical results

The numerical results presented in this section focus on two main aspects. The first one is concerned with the performance of the proposed model in dealing with shear locking. The second aspect is related to its ability to adequately represent boundary layers in plates and shells by using special functions.

6.1 Locking test

The locking phenomenon is a consequence of the inability of the approximation space to satisfy the natural restrictions for shear and membrane deformation as the thickness of the structural member goes to zero. Although more frequent in first order models, locking may appear in higher order models in the presence of deteriorated approximation spaces (severely distorted meshes, ill conditioned stiffness matrix, etc.). The symptom of this numerical pathology is an

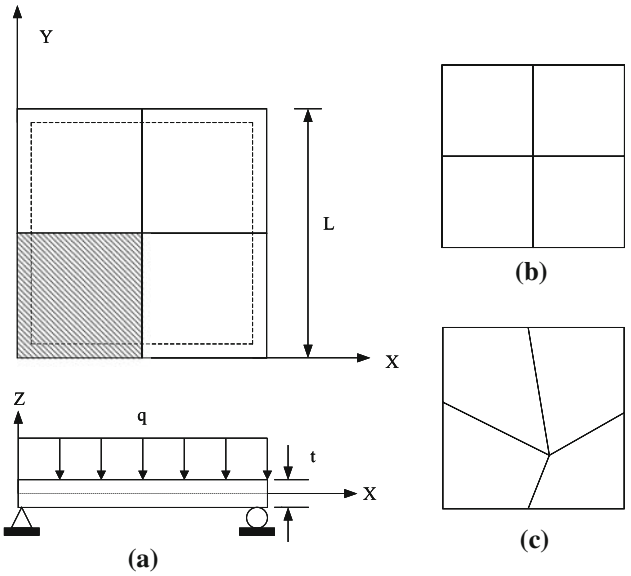

Fig. 11 **a** Simply supported square plate; **b** uniform mesh with four Q8 elements; **c** distorted mesh with four Q8 elements

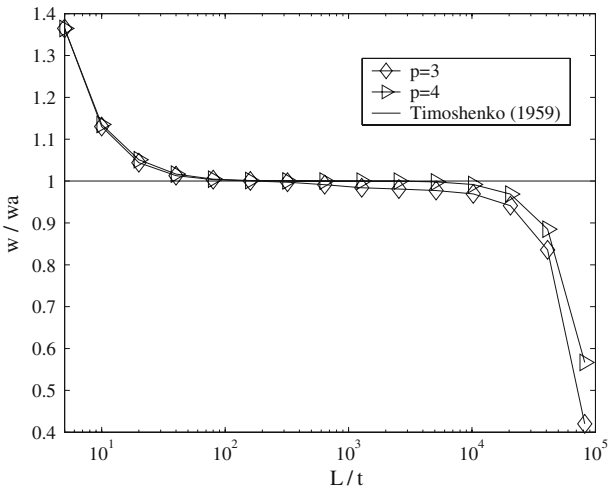

Fig. 12 Maximum transverse displacement, normalized by w/w_a, as a function of L/t, for uniform mesh

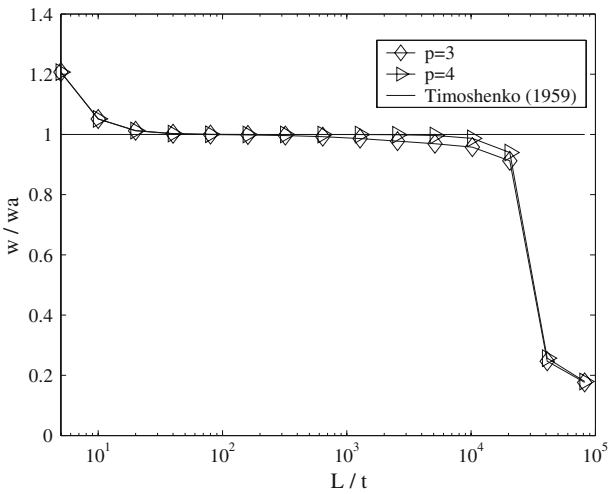

Fig. 13 Maximum transverse displacement, normalized by w/w_a, as a function of L/t, for distorted mesh

increase in the overall stiffness of the structure as the thickness goes to zero. Classical ways to circumvent this problem in conventional FEM are the selective sub-integration, as utilized, e.g., by Huang and Hinton [23] to avoid the membrane locking in the Scordelis–Lo cylindrical roof, and also by Belytschko et al. [7] in cylindrical shells under pinching loads. Other procedures have been used in conventional MEF: use of higher order elements [11] and p-adaptivity procedures [33], among others. In the case of meshless techniques, locking has been dealt with using nodal integration [9]; polynomials of different orders to approximate transverse displacements and rotations [13]; increasing the polynomial degree of the approximation functions [20]; using mixed formulation [12]; and, recently, constructing the approximation fields based on the reproduction of the Kirchhoff assumption as the shell thickness goes to zero [40].

In this example, the behavior of the GFEM with regard to the plate locking is evaluated considering the degree of the enrichment function as a variable. The Reissner–Mindlin kinematic model (27) is tested with a polynomial enrichment of the approximation space. The sensitivity to locking is evaluated with regard to mesh distortion considering two examples, both constituted by a square plate with simple hard supports, under uniformly distributed load, as shown in Fig. 11. The data is the following: length $L = 16$ mm, Young modulus $E = 2.1 \times 10^5$ MPa; thickness t variable, transverse load q [MPa] adjusted in such a way as to generate a maximum transverse displacement unchanged with the relation $L/t = 100$. Due to the symmetry of the problem, only a quarter of it is modeled. Two rough meshes are used, one uniform and one distorted, Fig. 11b and c, both modeled by four quadrangular elements, with the geometry mapped with 8 nodes (quadratic serendipity), referred to here as Q8.

Figures 12 and 13 show the transverse displacements normalized by the thin plate solution [38]. The results show the presence of locking, for the spaces built with polynomials $p = 3$ and $p = 4$, in the range $L/t \geq 10^4$. On the other hand, one observe that mesh distortion (Fig. 13) does not produce a deterioration of the approximation space severe enough to result in a large discrepancy with the results obtained with the uniform mesh.

6.2 Boundary layer phenomenon

The boundary layer phenomenon is characterized by a perturbation of the global solution in a narrow region close to the boundary. In plate and shell problems it is characterized

by an exponential decay of a physical field, like transverse shear, within a distance from the boundary of the order of the thickness of the shell.

For the specific case of Reissner–Mindlin models, the boundary layer effects are not associated with the transverse displacements, but with the rotations [2]. During the last decade, several proposals have appeared to approximate the behavior in the boundary layer. Babuska et al. [5] used p-hierarchic models; Xenophontos [41] utilize p- and hp-adaptivity to deal with the phenomenon; Cho and Oden [10] present a study about mesh optimization to capture the boundary layer utilizing a hierarchical model with a p-refinement of the mesh. The advances in localized problems have been notable due to the introduction of the meshless methods, which enable the incorporation of modes of the solution into the approximation spaces as studied by Duarte and Oden [14], Duarte [15], Duarte et al. [16], Duarte and Babuska [17] and Mendonça [34], among others. In all cases, as expected, the results are more accurate than those obtained with a polynomial basis only.

In the example shown next, the procedure outlined in Sect. 3.2 is applied to build local spaces that incorporate exponential-type functions along the considered boundary. These functions use modes of the analytical solutions given by Arnold and Falk [2] for these kinds of problems.

It is important to remark, however, that the strategy does not use the solution of a specific problem as the approximation space; instead, it uses characteristic modes, which are applicable to a given range of practical situations. To this aim, the local spaces are built using orthotropic enrichment as indicated in Eqs. (13)–(16). The high gradients of the solution along the normal direction of the boundary are represented with the aid of polynomial- and exponential-type functions (Fig. 8), while the solution along the tangent direction is treated by conventional polynomial approximations. This procedure aims to avoid the need for strong h-refinement of the mesh and to reduce considerably the number of degrees of freedom of the problem when compared with the uniform isotropic p-refinement.

In order to verify the performance of this proposition, some tests with plates and shells are described below. Numerical results in the cases of isotropic plates are compared with the analytical solutions presented by Arnold [2].

6.2.1 Plate with a free border, self-equilibrated load

The objective in this example is to test the accuracy of the computed shear force Q_y in a square plate made of elastic isotropic material (see Fig. 14). The plate is subjected to a transverse load varying sinusoidally in direction Y and constant in direction X. The data used is the following: length $L = \pi$ m; thickness $t = 0.02$ m; elastic modulus $E = 2.1 \times 10^{11}$ Pa and Poisson coefficient $\nu = 0.02$. Due to the symmetries, only the hatched part indicated in the figure is modeled with 2×16 quadrangular elements, integrated with 6×6 Gauss points in the interior elements and 31×31 points in the elements attached to the free border ($X = 0.0$). Finally, once the boundary functions are constructed for the clouds with prescribed degrees of freedom, the PU associated with the cloud is substituted by this function, together with all its products with the enrichments. It is verified that, applying the proposed technique to the example of Fig. 2, the correct solution is recovered.The results shown in Fig. 15 are graphs of the shear force Q_y evaluated along the dashed line (see Fig. 14) within a distance of 0.4 m from the border in comparison with the analytical solution of Arnold [2].

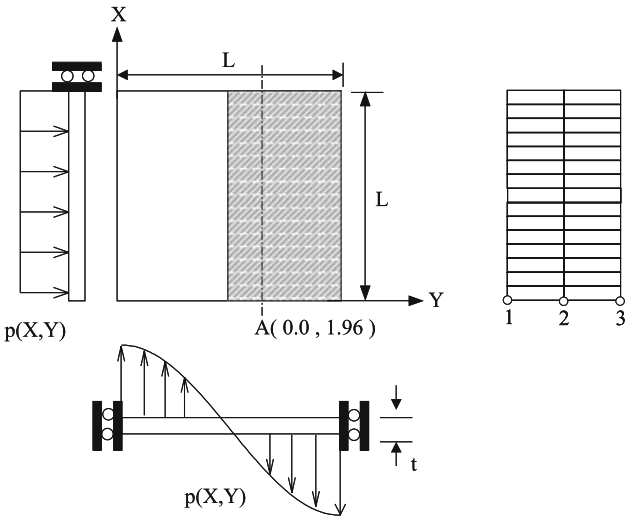

Fig. 14 Square plate with a free border ($X = 0$), subject to sinusoidal self-balanced load $p(X, Y) = q\cos(Y)$

Three different cases are tested:

Case A: Homogeneous isotropic refinement with polynomials of degree $p = 4$ for all clouds;

Case B: Orthotropic refinement with polynomials of degrees $p_x = 8$ and $p_y = 4$ (in directions x and y, respectively), for clouds 1, 2 and 3 (Fig. 14). The remaining clouds are enriched with $p = 4$;

Case C: Orthotropic refinement of type $(e^{\beta x}, p_y)$ with $p_y = 4$, $\beta = \sqrt{12k}$ and $k = 5/6$.

Table 3 Shear force Q_y at point A

Refinement	Q_y (N/m)	Error (%)
Case A	360.49106	34.5
Case B	541.94249	1.53
Case C	550.01692	0.063
Analytical	550.36329	

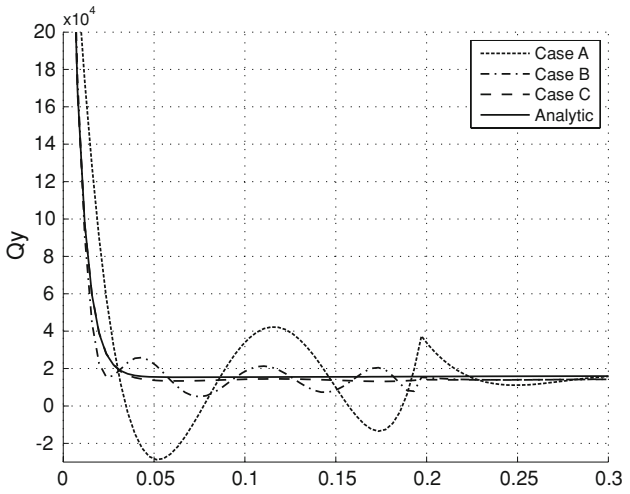

Fig. 15 Shear force Q_y (N/m) along axis X for cases A, B and C

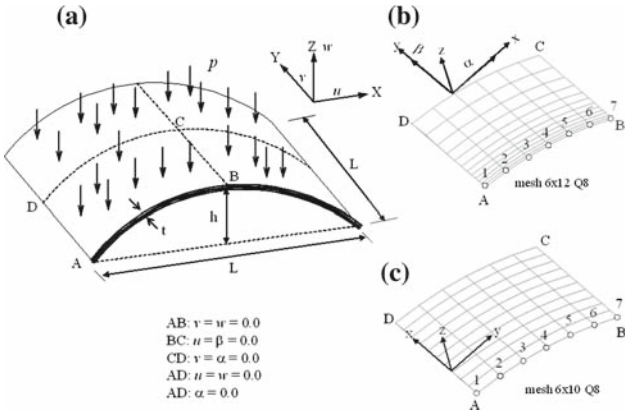

Fig. 16 **a** Shallow shell with vertical load uniformly distributed and boundary conditions; **b** adaptive mesh with 6 × 12 Q8 elements in decreasing geometric progression in direction AB, $r = 1.5$; **c** regular mesh with 6 × 10 Q8 elements

The values of Q_y at point A, $X = 0.0$, for the three cases and the analytical case is given in Table 3.

Results in Fig. 15 show oscillations when the enrichment is performed using polynomial functions only. Moreover, oscillations are more severe for Case A (homogeneous refinement) than for Case B (selective directional refinement). This is to be expected because the exact solution, although regular, presents steep gradients normal to the free border, making the homogeneous p-refinements less efficient (see Szabó and Babuska [36]). The strategy of Case B shows better accuracy at $X = 0.0$, although the quality is still poor because of the use of a polynomial basis and uniform mesh with element size one order larger than the plate thickness. The Case C, considering orthotropic enrichment with exponential functions shows excellent behavior compared with the other cases. The use of a local space adequate to this type of problem avoids oscillations near the boundary (Fig. 15) and gives very accurate local results close to the free end of the plate (Table 3).

6.2.2 Shallow parabolic shell

This example deals with a roof formed by a shallow parabolic shell (Fig. 16) subject to a vertical distributed load of 10^4 Pa. The material is homogeneous and isotropic with elasticity modulus $E = 2.1 \times 10^{11}$ Pa and Poisson coefficient $\nu = 0.3$. The geometric data is: length $L = 20$ m; width $L = 10$ m; height $h = 2.5$ m; thickness $t = 0.1$ m; Due to the symmetry, only the quarter ABCD is modeled. The accuracy of the shear force Q_y along the line CD is compared with a reference solution obtained by a hp-adaptive refinement. The adapted mesh is constituted by 6×12 elements with element size decreasing in geometric progression with rate $r = 1.2$ in direction Y from the border AB (Fig. 16b). The mesh used in the reference solution is isotropic, with polynomial functions with degree $p = 4$ for all clouds except those corresponding to nodes 1 to 7 (Fig. 16c), where the polynomial order is $p = 7$.

Table 4 Shear force Q_y at point A at the border AB

Refinement	Q_y (kN/m)	Error (%)
Case A	3939.88	35.8
Case B	5926.58	3.45
Case C	6265.03	−2.06
Reference	6138.35	

The results shown in Fig. 17 were calculated using the uniform mesh shown in Fig. 16c. The local values for shear force at point A of border AB are shown in Table 4. Three strategies of p-adaptivity are tested with the following characteristics:

Case A: Homogeneous isotropic refinement with $p = 4$;
Case B: Orthotropic refinement with $p_x = 4$ and $p_y = 7$ for clouds 1–7. All the remaining clouds are isotropically enriched with $p = 4$.
Case C: Orthotropic refinement $(e^{\beta \bar{x}/t}, p_y)$, with $p_y = 4$, for clouds corresponding to points 1-7 (Fig. 16c). The remaining clouds are enriched with $p = 4$; $\beta = \sqrt{12k}$ and $k = 5/6$.

The results observed in Fig. 17 highlight the quality of the local spaces corresponding to Case C. The local effect of the exponential function in the orthotropic refinement results in values close to the reference solution, without the oscillations characteristic of the spaces based only on polynomials (Cases A and B). Although the orthotropic refinement of strategy B results in smaller amplitudes and values closer to the reference solution than those obtained with strategy A, this family of functions is not able to avoid the oscillatory phenomenon close to the border.

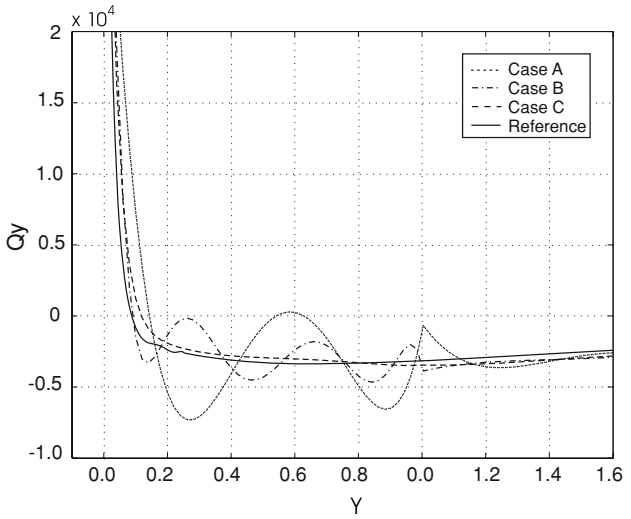

Fig. 17 Shear force Q_y (N/m) along corner AD for the first five elements

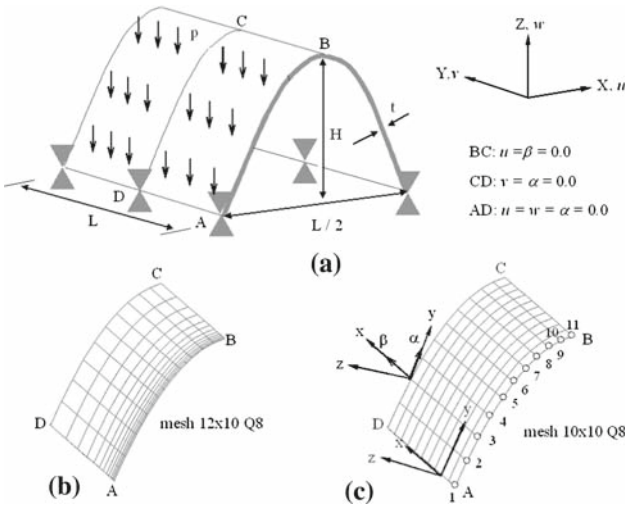

Fig. 18 Parabolic shell with high curvature, under vertical load uniformly distributed

6.2.3 Parabolic shell with large curvature

This example shows a parabolic roof with a large curvature subject to a uniformly distributed vertical load of 1.0×10^4 Pa (Fig. 15). The geometric and material properties are: length and width have the same value $L = 20$ m; height $H = 10$ m; thickness $t = 0.10$ m; elastic modulus $E = 3.1906872 \times 10^{10}$ Pa; coefficient of Poisson $\nu = 0.33$. Due to the symmetry only the quarter ABCD is modeled. Similarly to the previous case, this problem also presents a boundary layer in the shear forces near point A, within a distance of the order of the thickness from the border. Three strategies of p-enrichment are tested for a regular mesh of 10×10 elements:

Case A: Isotropic homogeneous refinement with $p = 4$.
Case B: Orthotropic refinement with $p_x = 7$ and $p_y = 4$, for clouds corresponding to points 1-11. For all the remaining clouds the refinement is isotropic with $p = 4$.
Case C: Orthotropic p-refinement of type $(e^{\beta \bar{x}/t}, p_y)$, with $p_y = 4$, for clouds corresponding to points 1-11 (Fig. 18c). For all the remaining clouds, the refinement is isotropic with $p = 4$.

Since there is no known analytic solution to the problem, the comparisons are made with a reference solution obtained by *hp*-adaptive refinement. In this case, the mesh is constituted by 12×10 elements in geometric progression with rate $r = 1.3$ in direction AB. The p-refinement is the same used in Case A. The shear force at point A is shown for all cases in Table 5.

The behavior of the results in Fig. 19 is analogous to that of the previous example. The strong oscillations corresponding to the polynomial refinements in strategies A and B emphasize the difficulty of this family of functions to adequately represent the behavior of the solution within the boundary layer. However, one can note that an adequate enrichment, with exponential decay, is sufficient to avoid the oscillations.

Table 5 Shear force Q_y (N/m) at point A

Refinement	Q_y (N/m)	Error (%)
Case A	49512.01	40.8
Case B	71235.82	14.9
Case C	75042.05	10.3
Reference	83700.83	

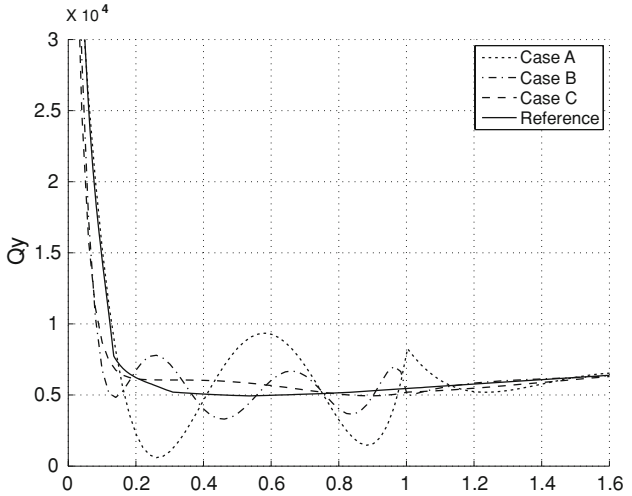

Fig. 19 Shear force Q_y (N/m) along the first three elements on the corner DA adjacent to node A

7 Conclusions

In this paper, two main contributions were presented in order to extend the use of GFEM techniques to shell problems. The first one is a way of defining local domains for function enrichments based on the use of pseudo-tangent planes. The second one is the inclusion of special functions for the treatment of homogeneous essential boundary conditions and local behaviors, commonly named *boundary layer problems*. A set of examples were selected in order to show the behavior of the proposed strategies, whose results were commented along the text. A group of final remarks sum up important observations obtained from this work:

- The technique of constructing the enrichment functions on a pseudo-tangent plane showed good results. It is clear that the larger the shell curvature, the more distorted the enrichment functions become due to the coordinate transformations. However, all studied cases show good results even in most curved cases.
- Although no specific strategies to deal with locking were included, the method behaves in a similar way as observed in classical hierarchical FEM methods, i.e., avoiding locking for appropriate p-refinement values and within thickness ranges of practical interest.
- Essential boundary conditions were imposed in strong form more efficiently than with penalty or Lagrange multiplier methods, avoiding significative extra calculations. Moreover, it appear to be a convenient choice to capture perturbed values along these boundaries.
- One of the claimed characteristics of the GFEM technique is the easiness to include special customized functions. The inclusion of exponential modes for the treatment of boundary layers in shells provided extremely good results. Accurate and non oscillating solutions were obtained even with elements many times larger than the thickness of the shell. It should be noted, however, that not every boundary layer shell phenomenon will be adequately treated with the exponential mode used here, and other specialized modes should be included in the set of functions available.
- As in every p enrichment method, the number of integration points is associated with the complexity of the enrichment function. When polynomials are used, these integration points are conveniently distributed along the element following appropriate quadrature rules. On the other hand, if special functions for boundary layer cases are included, most of the function information is concentrated in a region close to the boundary. Thus, the quadrature rule for them should follow this characteristic and coordinate changes for quadrature rules like that proposed by Telles [39] may be used.
- It is important to note that the pseudo-tangent plane and the strategies proposed based on special functions are neither related to the particular cinematic model used in this work (Mindlin–Reissner) nor to the geometric shell representation. The main idea behind the pseudo-tangent plane proposition is to separate the geometry description and its intrinsical distortions with respect to the physical domain, from the approximation space. Although in present computations the shell geometry is defined by classical element mappings, other geometry intrinsical descriptions may be used in a totally independent way.
- The imposition of essential boundary conditions deserves some further comments. The Lagrange multipliers method, the penalty method and the Nitsche's method impose approximations to the prescribed value on the boundary. Stability in the Nitsche's method requires the choice of a stabilization parameter (see [19]) and an incorrect choice for this factor can lead to precision loss in the imposed values on the boundary. However, the most important restriction on this method is that the necessary modification of the weak form is different for each particular problem [31]. In the boundary layer problems, where the high gradients occur near the boundaries with prescribed displacements, it is considered important to be able to impose these values in a very precise way. The proposed procedure fulfill this requirement, with good accuracy in the stresses, and without oscillations in the response in all cases analyzed. This is obtained with a minor cost increase: the process of generating the approximation functions on the boundary by multiplication of the partition of unity functions by ramp functions, increases the polynomial degree of the resulting functions. This requires a larger number of Gauss points in the integration of the border functions in relation of the interior functions. However, this is restricted to the elements attached to the boundary and not to the whole mesh.

References

1. Ahmad S, Irons BM, Zienkiewicz OC (1970) Analysis of thick and thin shell structures by curved finite element. Int J Numer Method Eng 2:419–451
2. Arnold DN, Falk SR (1989) Edge effects in the Reissner–Mindlin plate theory, analytic and computational models of shells 10-15-1989, A.S.M.E., New York
3. Babuska I, Banerjee U, Olborn JE (2002) Meshless and generalized finite element methods: a survey of some major results. In: Schweitzer MA, Hildebrandt S (eds) Meshfree Methods for partial differential equations, International Workshop, University of Bonn, Garmany, 11–14 September. Lecture Notes in Computational Science and Engineering, Springer, Berlin, pp 1–20
4. Babuska I, Melenk JM (1996) The particion of unity finite element method: basic theory and applications. Comput Methods Appl Mech Eng 139(1–4):289–314

5. Babuska I, Szabó B, Actis R (1990) Hierarchic Models for Composite Laminates; Report WU/CCM-90/4, Center for Computational Mechanics, Washington University, St. Louis, Missouri
6. Belytschko T, Black T (1999) Elastic Crack Growth in Finite Elements with Minimal Remeshing. Int J Numer Methods Eng 45:601–620
7. Belytschko T, Liu WK, Ong JSJ, Lam D (1985) Mixed variational principles and stabilization of spurios modes in the 9-nodes elements. Comput Struct 20:121–128
8. Belytschko T, Lu YY, Gu L (1994) Element free Galerkin method. Int J Numer Methods Eng 37:229–256
9. Beissel S, Belytschko T (1996) Nodal integration for element-free Galerkin method. Comput Methods Appl Mech Eng 139(1–4):49–74
10. Cho J-R, Oden JT (1997) Locking and boundary layer int hierarchical models for thin elastic structure. Comput Methods Appl Mech Eng 149:33–48
11. Della Croce L, Scapolla T (1992) Hierarchic finite element method with seletive and uniform reduced integration for Reissner-Mindlin plates. Comput Mech 10:121–131
12. Dolbow J, Belytschko T (1999) Volumetric locking in the element-free Glerkin method. Int J Numer Methods Eng 46:925–942
13. Donning BM, Liu WK (1998) Meshless method for shear-deformable beams and plates. Comput Methods Appl Mech Eng 152(1–2):47–71
14. Duarte CA, Oden TJ (1996) Hp-clouds—an h–p meshless method. Numér Methods Partial Differ Equ 12:673–705
15. Duarte CA (1996) The hp clouds methods, Phd Tesis, Austin, Texas
16. Duarte CA, Babuska I, Oden JT (2000) Generalized finite element method three dimensional structural mechanics problems. Comput Struct 77:215–232
17. Duarte CA, Babuska I (2002) Mesh-independent directional p-enrichment using the generalized finite element method. Int J Numer Methods Eng 55:1477–1492
18. Ferreira AJM, Roque CMC, Jorge RMN (2007) Natural frequencies of FSDT cross-ply composite shells by multiquadric. Compos Srtuct 77:296–305
19. Fritz A, Hueber S, Wohlmuth BI (2004) A comparison of mortar and Nitsche techniques for linear elasticity. Calcolo 41:115–137
20. Garcia O, Fancello EA, Barcellos CS, Duarte CA (2000) hp-Clouds in Mindlin's thick plate models. Int J Numer Methods Eng 47(8):1381–1400
21. Garcia OA (2003) (Elementos finitos generalizados na análise estática de placas e cascas.) Doctoral Thesis. Department of Mechanical Engineering, Federal University of Santa Catarina - UFSC., Florianópolis
22. Griebel M, Schweitzer MA (2002) A particle-partition of unity method. Part V: Boundary conditions. In: Hildebrandt S, Karcher H (eds) Geometric analysis and nonlinear partial differential equations. Springer, Berlin pp 517–540
23. Huang CA, Hinton E (1986) A new nine node degenerated shell element with enhanced membrane and shear interpolation. Int J Numer Methods Eng 22:73–92
24. Krysl P, Belytschko T (1996) Analysis of thin shells by the element-free Galerkin method. Int J Solids Struct 33(20–22):3057–3080
25. Kansa EJ (1990) Multiquadrics-a scattered data approximation scheme with application to computational fluid dynamics. I: Surface approximation and partial derivative estimates. Comput Math Appl 19(8–9):45–127
26. Kansa EJ (1990) Multiquadrics-a scattered data approximation scheme with applications to computational fluid dynamics II: Solution to parabolic, hyperbolic and elliptic partial diferential equations. Comput Math Appl 19(8–9):92–385
27. Liu L, Chuan LP, Ghesta DM (2006) Conforming radial point interpolation method for spatial shell structures on the stress-resultant shell theory. Arch Appl Mech 75:248–267
28. Li S, Hao W, Liu WK (2000) Numerical Simulations of large deformation of thin shell using meshfree methods. Comput Mech 25:102–116
29. Liu WK, Jun S, Zhang YF (1995) Reproducing kernel particle method. Int J Numer Methods Fluids 20:1081–1116
30. Melenk JM, Babuska I (1996) The partition of unity finite element method: basic theory and applications. Comput Methods Appl Mech Eng 139:289–314
31. Mendez SF, Huerta A (2004) Imposing essential boundary conditions in meshfree methods. Comput Methods Appl Mech Eng 193:1257–1275
32. Moes N, Dolbow J, Belytschko T (1999) Elastic crack growth in finite elements without remeshing. Int J Numer Methods Eng 46:131–150
33. Novotny A, Fancello EA (1996) Estudo das versoes adaptativas h, p e hp do método Método de Elementos Finitos na análise de flexão de placas de Reissner–Mindlin; Monografia de iniciação científica; Grupo de Análise de Tensões, UFSC
34. Mendonça PTR, de Barcellos CS, Duarte CA (1998) Investigations on Timoshenko Beam Problems Using the hp-Clouds Meshless FEM. In: IV World Congress on Computation Mechanics, Buenos Aires, Argentina
35. Oden TJ, Duarte CA, Zienkiewicz OC (1998) A new cloud-based hp finite element method. Comput Methods Appl Mech Eng 153:117–126
36. Szabó B, Babuska I (1991) Finite element analysis. Wiley, New York
37. Schwebke KG, Holzer SM (2002) Some remarks on generalized finite element methos (GFEM) in solid mechanics, WCCM V. In: Fith World Congress on Computational Mechanics, Viena, Austria
38. Timoshenko SP, Woinowsky-Krieger S (1959) Theory of Plate and Shells, 2nd edn. Macgraw-hill, New York
39. Telles JCF (1987) A self-adaptative co-ordinate transformation for eficient numerical evalutation of general boundary element integrals. Int J Numer Methods Eng 24:959–973
40. Tiago C, Leitão V (2005) On the procedures to eliminate shear locking in the meshless methods, ECOMAS. In: Tematic conference on meshless methods
41. Xenophontos CA, Schwab C, Suri M (1996) The hp version of the finite element method for singulary perturbed problems, Dissertation submitted to the graduate school of the University of Maryland in partial fulfillment of the requeriment for the degree of Doctor of Philosophic
42. Zhu T, Atluri SN (1998) A modified collocation method and a penalty formulation for enforcing the essential boundary conditions in the element free Galerkin method. Comput Mech 21(3):211–222